ELSEVIER

Stress-dependent molecular pathways of silica–water reaction

Ting Zhu[a], Ju Li[b], Xi Lin[c], Sidney Yip[c,d],*

[a]*Department of Mechanical Engineering, Massachusetts Institute of Technology, Cambridge, MA 02139, USA*
[b]*Department of Materials Science and Engineering, Ohio State University, Columbus, OH 43210, USA*
[c]*Department of Nuclear Science and Engineering, Massachusetts Institute of Technology, Cambridge, MA 02139, USA*
[d]*Department of Materials Science and Engineering, Massachusetts Institute of Technology, Cambridge, MA 02139, USA*

Abstract

Stress-corrosion of silica by water is studied by exploring the stress-dependent potential energy surface computed quantum mechanically at the level of molecular orbital theory. An ordered silica nanorod with clearly defined nominal tensile stress is constructed to model a structural unit of the stressed crack tip. Three competing hydrolysis reaction pathways are determined, each involving a distinct initiation step. Water dissociation, molecular chemisorption, and direct siloxane bond rupture dominate at low, intermediate, and high stress levels, respectively. A linear stress dependence in the thermodynamic driving force, not commonly considered in the criterion of brittle fracture initiation, is shown to originate from surface relaxation associated with bond rupture. This effect is particularly important in determining the Griffith condition of crack extension for nano-sized systems when spatial accommodation of foreign molecules is involved in the process of bond breaking. The physical

*Corresponding author. Tel.: + 1 617 253 3809; fax: + 1 617 258 8863.
E-mail address: syip@mit.edu (S. Yip).

origin of the stress dependence of kinetic barrier is revealed by a perturbation analysis of the minimum energy path parametrized by the continuous mechanical stress.

1. Introduction

Chemical reaction rates in solids are known to depend on mechanical stress levels (e.g., see Hillig and Charles, 1964; Lawn, 1993; Gilman, 2003). This effect can be generally described in terms of a change of activation energy barrier in the presence of stress. A typical example is stress corrosion of silica glass by water; the strength of the glass decreases with time when subjected to a static load in an aqueous environment (Wiederhorn, 1967). The phenomenon, also known as delayed failure or static fatigue, essentially refers to the slow growth of pre-existing surface flaws as a result of corrosion by water in the environment. From a microscopic viewpoint (Michalske and Freiman, 1982, 1983), it is believed that the intrusive water molecules chemically attack the strained siloxane (Si–O–Si) bonds at the crack tip, causing bond rupture and formation of terminal silanol (Si–OH) groups which repel each other at the conclusion of the process. This molecular level mechanism, intrinsically, governs the macroscopic kinetics of quasi-static crack motion.

One of the earliest chemical theories of brittle fracture was put forward by Orowan (1944), who extended Griffith's concept of the equilibrium crack to water-assisted crack growth by considering environmental effects on surface energy reduction. Within a more general framework of irreversible thermodynamics, Rice (1978) derived an inequality governing the relation between crack extension rate and associated thermodynamic driving force in a chemically reactive environment. This relation is essentially a global restriction on the detailed molecular kinetics of crack growth. From a kinetics perspective, Hillig and Charles (1964) considered stress-enhanced thermal activation processes and formulated an Arrhenius-type relation to describe the corrosion rate based on reaction rate theory. This model was applied by Wiederhorn (1967) to correlate measured crack velocity with applied load, as well as extended by Chuang and Fuller (1992) to study the morphological evolution of a notch tip and its implication for stress corrosion cracking.

A full understanding of stress corrosion in silica glass must also consider molecular mechanisms and quantitative characterization of reaction kinetics. On the basis of molecular orbital theory, Michalske and Freiman (1982, 1983) have proposed a molecular interpretation of stress corrosion in vitreous silica. The chemical interaction between the intrusive water molecule and strained siloxane bonds is envisaged to proceed in a three-step sequence, adsorption, reaction and separation. By considering the electron and proton-donating capacity of the intrusive chemical species and the polarity of the bridging bond, the Michalske and Freiman (MF) model explained why water and other chemical species such as

ammonia could be effective in promoting crack growth. The effect of stress on chemical reactivity of solids was addressed in a follow-up calculation (Michalske and Bunker, 1984), where it was suggested that bond angle deformations are most effective in increasing the chemical reactivity; in particular, stress-induced pinching of the O–Si–O bond angle can form a chemically active kink site. In contrast to directly imposing deformation on a siloxane ring, calculated reactivities of various membered cyclosiloxane rings have been compared by West and Hench (1994), resulting in quantitative reaction pathways for three- and four-fold silica rings and a five-fold ring-chain structure. Three-membered rings are found to be more chemically reactive due to the lower energy barrier associated with larger ring strains. The study of chemical reactivity of different ring structures is also useful in understanding the kinetics of hydrolyzing silica surface where various types of ring structures exist due to surface reconstruction (e.g., see Walsh et al., 2000; Du et al., 2003). To our knowledge, no systematic studies have been carried out on the variation of water–silica reaction barriers with mechanical stress.

In this paper, we present a detailed investigation of the stress-enhanced hydrolysis reaction using a model system of a single water molecule interacting with a silica nanorod. We first construct the nanorod, to be detailed in the next section, as a representative structural unit cut from a crack tip, and then study the unit process of hydrolyzing a stretched siloxane bond at the surface of the nanorod. We rely on this unit-process study to quantify the problem of stress corrosion at a crack tip through the assumption that the intrusive water molecules have a direct access to individual siloxane bonds at the crack tip. In other words, we assume the crack-tip hydrolysis reaction is the rate-limiting step for stress corrosion, and that all other transport processes, such as bulk diffusional flow and water diffusion along the fractured surfaces, are relatively fast. Our bond-saturated nanorod is constructed as a mechanically meaningful structure, in contrast to the commonly used model clusters, e.g., $H_6Si_{18}O_7$ by Lindsay et al. (1994); its major characteristic is structural uniformity, which allows meaningful definitions of stress and strain. Thus we are able to explicitly map out families of reaction pathways, parametrized by the continuous nominal stress. It follows that analysis of the stress-mediated reaction pathways reveals the role of stress in both the thermodynamic driving force and kinetic barriers for the hydrolysis reaction. Such an analysis, we believe, is a step closer toward a unified description of the thermodynamics and the kinetics of quasi-static crack extension in silica glass.

2. Model and method

2.1. Nanorod structure

We show in Fig. 1(a) a silica nanorod composed of 108 atoms (36 SiO_2 units) (Zhu et al., 2003, 2005; de Leeuw et al., 2003). Our construction of a nanorod first involves the formation of planar six-membered rings, Si_6O_{18}. As shown in Fig. 1(b), each Si_6O_{18} ring contains six corner-linked SiO_4 tetrahedra, where each tetrahedron has
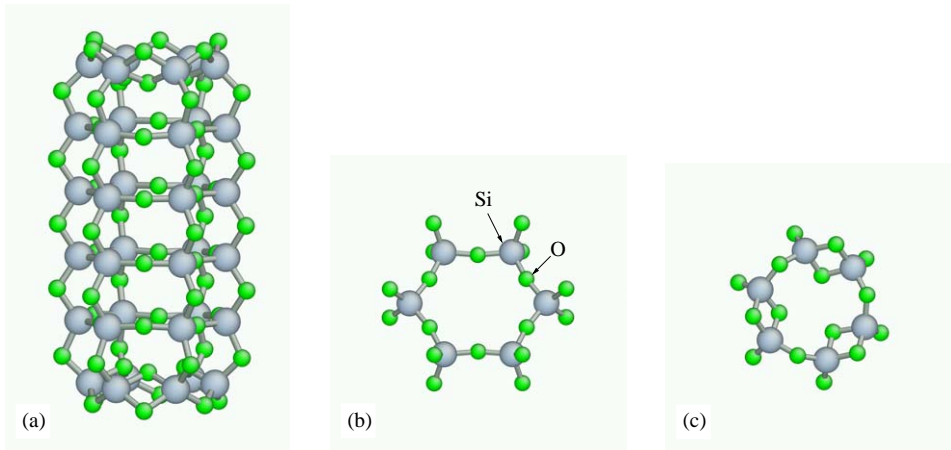
Fig. 1. Structure of (a) a relaxed nanorod, (b) an interior ring, and (c) an end ring.

two bridging oxygen atoms that are shared with two neighboring tetrahedra. The nanorod is then assembled by stacking such rings (layers) one over another to form a rod-like network of SiO_4 tetrahedra. For the structure to be free from dangling bonds, the nanorod is capped at the ends by 'terminating' rings in which the six Si atoms are connected alternately by a bridging oxygen or two oxygens, in the manner shown in Fig. 1(c). The resulting structure is a stoichiometric silica nanorod with the bulk built up of corner-sharing SiO_4 tetrahedra, where all Si and O atoms are four- and two-coordinated, respectively, but capped by three pairs of edge-sharing SiO_4 tetrahedra at each end. The size and geometry of the nanorod are similar to the channels in α-quartz and the outer wall of the rod resembles the α-quartz $(0\,0\,0\,1)$ surface, where all Si and O atoms are fully coordinated without dangling bonds. Moreover, the hexagonal planar six-membered rings of the nanorod exist in natural cyclosilicate minerals such as beryl which contains those rings linked by Be^{2+} and Al^{3+} ions (Kim et al., 1995).

2.2. Force field

The study of the stress-enhanced hydrolysis reaction entails a proper description of interatomic interactions. Empirical potentials have been proven to have deficiency in treating correctly the effects of charge transfer when bonds are broken and formed. On the other hand, it is very computationally expensive to apply the first-principles quantum mechanical calculation to explore various reaction pathways under different stress states. As a reasonable compromise between accuracy and efficiency, we choose to use the semi-empirical molecular orbital theory method in our study. The energies for different nanorod configurations given below are calculated using MOPAC 2000 (Stewart, 2002) with the PM3 method (Stewart, 1989). A comparison study for the hydrolysis reaction of various silica clusters between calculations of the density functional theory (DFT) and the semi-empirical

molecular orbital theory (AM1 and PM3) has been given by Laurence and Hillier (2003). They found that both the optimized structures and transition states (for interaction with a single water molecule) from molecular orbital methods are qualitatively similar to those obtained via DFT calculations, though there exist some quantitative differences. Considering that the molecular orbital theory calculation is significantly faster than the high-level first-principles calculation, we apply the semi-empirical method as our first step to explore stress-mediated reaction pathways.

2.3. Mechanical deformation

Mechanical deformation of the nanorod is imposed via the displacement control method. We use 15 atoms in each end-ring as grips, with each atom given a prescribed displacement in the axial direction of the rod, and all other atoms are allowed to relax using the conjugate gradient method. To characterize the stress state of the nanorod we take the sum of all forces acting on the cross-section divided by the nominal cross-section area $A_0 = 4\pi d_{OO}2 = 88.9\,\text{Å}^2$ where d_{OO} denotes the side length of a SiO_4 tetrahedron and it is also the edge length of the hexagon composed of six bridging O's within the planar six-membered ring. The nominal cross-section of the nanorod is taken as the circle enveloping a hexagon with a radius $R = 2d_{OO}$. To measure the tensile strain applied to the nanorod, we take the elongation of the rod divided by the initial gage length (distance between two grips) $L_0 = 4d_{OO} = 10.6\,\text{Å}$.

2.4. Finding reaction pathway and transition state

The study of kinetics of the stress-mediated hydrolysis reaction is carried out within the framework of transition state theory (TST) (Vineyard, 1957). The problem then becomes that of identifying the reaction mechanism and finding the free energy barrier. Within the harmonic approximation to TST, the problem is further reduced to finding a minimum energy path (MEP) on the (electronically) adiabatic potential energy surface (PES). The MEP is defined as a continuous path in a $3N$ dimensional configuration space (where N is the number of free atoms) with the property that at any point along the path, the atomic forces are zero in the $3N - 1$ dimensional hyperplane perpendicular to the path (see Sorensen et al., 2000, for example). The energy maximum along the MEP is the saddle-point energy which gives the activation energy barrier. Since the PES will evolve with stress, the stress-mediated kinetics manifests itself as a stress-dependent activation energy barrier.

The MEPs of hydrolysis reactions are calculated using the nudged elastic band (NEB) method (Jónsson et al., 1998; Henkelman and Jónsson, 2000). Prior to NEB calculations, we first identify a physisorbed state which corresponds to a local energy minimum along the reaction pathway. Here, physisorption refers to the process of hydrogen bond formation between the H_{wat} of the water molecule and the bridging O_{br} of the nanorod. During physisorption, there is no real chemical bond rupture and/or formation. In contrast, the hydrolysis reaction is a chemisorbed process since

it involves the dissociation of the water molecule as well as the formation of new chemical bonds, i.e., silanol surface groups.

Each NEB calculation proceeds in the following two steps: We first calculate the physisorption pathway by choosing an initial state where the water molecule is separated from the stressed nanorod by about 15 Å. The final state is one of the physisorbed states, all the while keeping the extension of grip ends the same as that of the initial state. Then the chemisorption pathway is located by choosing as two endpoints the initial physisorbed state and the final chemisorbed state, respectively. The elastic band consists of seven equally spaced replicas of the system forming a discretized path between two fixed endpoints. The calculation is considered converged when the force on each replica is less than 0.05 eV/Å. A continuous MEP is then obtained by cubic polynomial interpolation of the calculated energies with the aid of the potential force projected in the direction of the path on each replica (Henkelman and Jónsson, 2000). Since the spacing between adjacent replicas is fixed during NEB relaxation, the transition state may not be coincident with any of the relaxed replicas. Hence we show the transition state in Section 3 using the relaxed replica closest to the saddle point. Additionally, for the same set of initial and final states, there may exist several competing reaction pathways corresponding to different reaction mechanisms. As the potential energy landscape evolves with stress, the same type of the initially guessed path, e.g., a linear interpolation of intermediate replicas between two endpoints, may relax to distinct pathways at different stress levels. Therefore, in order to follow the evolution of the same transition mechanism with increasing stress, we first identify one pathway of interest at zero stress. Then, in all subsequent NEB calculations at other stress levels, the final relaxed pathway from a previous search will be taken as an initial input for relaxation at a new stress level, but note that the system will be uniformly scaled according to the current extension of the nanorod. Since the external loading is applied via the displacement-control method, during each NEB relaxation, we keep the positions of atoms at grip ends for all the intermediate replicas fixed at those of the initial state. The tensile stress within the nanorod in the initial state is then taken as the nominal stress to label the calculated activation energy barrier.

3. Results

3.1. Uniaxial tension of dry and hydrolyzed nanorods

The stress–strain response for uniaxial tension of a nanorod without water is first calculated as shown in Fig. 2 by the solid line. It is seen that the nanorod deforms linearly in the early stages. The corresponding Young's modulus is about 189 GPa. Then the stress–strain variation shows a slight nonlinearity up to the point of failure where the stress drops precipitously. The breaking stress at the onset of failure, denoted by σ_{cr}, is about 55.2 GPa and the corresponding critical strain, ε_{cr}, is 0.36. The value of σ_{cr} represents the athermal mechanical strength of the nanorod, i.e., the maximum resistance to fracture without the aid of thermal fluctuations. σ_{cr} will be
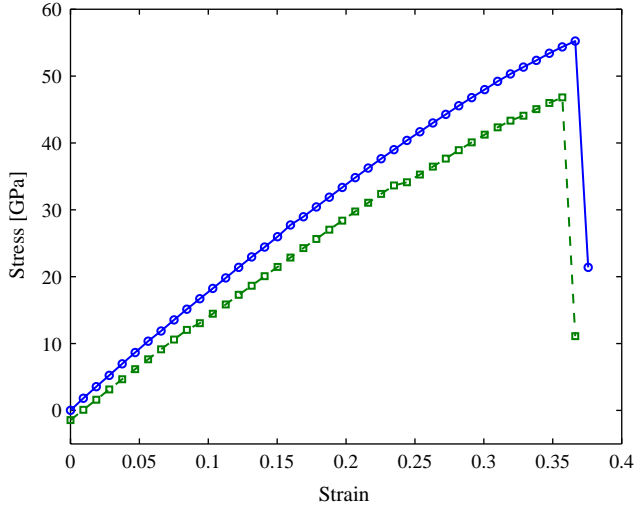
Fig. 2. Stress vs. strain curves for uniaxial tension of the dry nanorod (solid line) and the hydrolyzed nanorod (dashed line). Circles and squares are calculated data points.

used later as a strength-normalizing parameter for the calculated activation energy barriers at different stress levels.

We show next that our definitions of the nominal cross-section and stress on the nanorod are mechanically meaningful. Note that the nanorod was constructed with siloxane bonds uniformly aligned along the axial direction, leading to bond directionality as well as structural periodicity in this direction. Thus, we expect that the mechanical property of the rod should be closer to that of crystalline quartz along an orientation with a similar atomic arrangement, though an exact structural mapping does not exist between the two systems. We have compared the nominal values of Young's modulus, σ_{cr}, and ε_{cr} of the rod with those of the bulk quartz. A slight complication is that bulk quartz undergoes an $\alpha \to \beta$ transition when uniaxially pulled at about 5 GPa stress. Since the β-phase spans most of the uniaxial strain range till failure, and is significantly stiffer than the α-phase, we take the β-quartz as reference, whose Young's modulus is around 180 GPa for both $(0\,0\,0\,1)$ and $(1\,1\,\bar{2}\,0)$ stretching (Liao, 2001). In $(0\,0\,0\,1)$ uniaxial stretching, β-quartz fails at $\sigma_{cr} \approx 58$ GPa and $\varepsilon_{cr} \approx 0.34$. In $(1\,1\,\bar{2}\,0)$ uniaxial stretching, β-quartz fails at $\sigma_{cr} \approx 42$ GPa and $\varepsilon_{cr} \approx 0.25$. Both sets of values are close to those of the nanorod. In addition, we note that comparing to silica fibers (Proctor et al., 1967; Kurkjian et al., 2003) that consist of a continuous random network of SiO_4 tetrahedra, the nanorod with uniformly aligned siloxane bonds has larger values of Young's modulus and breaking stress.

As the inter-ring siloxane bonds are the primary load carriers, we report on the geometric changes of a representative inter-ring siloxane bond located in the middle section of the nanorod. The calculated Si–O bond length prior to bond rupture is 1.827 Å compared to a value of 1.686 Å at the fully relaxed state. Correspondingly, the Si–O–Si bond angle changes from the initial value of 114.3° to 146.0°.

We also show in Fig. 2 (dashed line) the uniaxial stress–strain response of a hydrolyzed nanorod. The atomic structure of the hydrolyzed nanorod with silanol surface groups is shown in Fig. 4(d). Similarly, the stress increases almost linearly with the applied strain, but with a lower Young's modulus of 154 GPa. We note that there exists a compressive stress of about 1.44 GPa within the hydrolyzed nanorod at zero strain. This residual stress at zero strain arises from a repulsive interaction between two fully relaxed silanol groups. As will be demonstrated later, the existence of residual stress in the hydrolyzed nanorod will lead to a term linearly dependent on the applied load in the thermodynamic driving force of the hydrolysis reaction. In particular, this term has important implications for understanding the critical condition of brittle fracture initiation.

3.2. Thermodynamics of physisorption and chemisorption

Physisorption involves the formation of two hydrogen bonds with two bridging oxygen atoms (O_{br}) of the nanorod. We identify two physisorbed states. One corresponds to an asymmetric binding configuration with different hydrogen bond lengths as shown in Fig. 4(b). At zero stress, the calculated bond lengths are 1.75 and 2.50 Å, respectively. Another physisorbed state takes a symmetric binding form as shown in Fig. 6(b). The two hydrogen bond lengths at zero stress are both 1.79 Å. The energy change associated with physisorption is defined as the hydration energy E_{hydr} of the nanorod (de Leeuw et al., 2003). That is,

$$E_{hydr} = E_{rod+wat}^{p} - (E_{rod} + E_{wat}), \qquad (1)$$

where $E_{rod+wat}^{p}$ is the total energy of the rod with a physisorbed water molecule, E_{rod} the energy of the nanorod without water, but under the same stress as the hydrated nanorod, and E_{wat} the self-energy of a single water molecule. At zero stress, the values of E_{hydr} for the asymmetric and symmetric binding forms are −0.57 and −0.63 eV, respectively. Comparing the two physisorbed states, it is evident that the lower hydration energy leads to stronger hydrogen binding as indicated by a shorter hydrogen bond length. We also calculate the hydration energy as a function of stress and find that stress only affects hydration energies weakly for both of the physisorbed states. Take the asymmetrically adsorbed state as an example. As the stress increases to about 35 GPa, the hydration energy only reduces by about 0.03 eV down to −0.60 eV. In addition, we also calculate MEPs of physisorption and find that no saddle point exists irrespective of stresses. Therefore, physisorption of a single water molecule to the silica nanorod is a thermodynamically favorable process without kinetic barrier.

In contrast, chemisorption involves the formation of two silanol surface groups. At a given stress level, the relaxed structure of the hydrolyzed nanorod may take various configurations with different arrangements of relative positions of the two silanol groups. These geometrically similar states correspond to local minima with very close energies on the same PES. To examine the effect of stress, we focus on a representative type of the relaxed structure as shown in Figs. 4(d), 6(f) and 8(d). This chemisorbed structure will later be taken as the final state in NEB calculations to
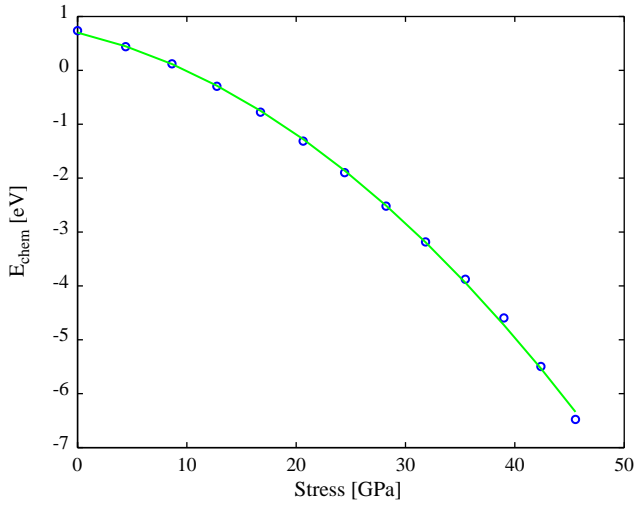
Fig. 3. Stress-dependent chemisorption energy. Circles are the calculated data points and the solid line is the result of the polynomial fitting given by Eq. (3).

identify various pathways of hydrolysis. Define the chemisorption energy E_{chem} as the difference in the total energy between the chemisorbed state $E_{rod+wat}^c$ and the water-nanorod non-interacting state at the same stress level. That is,

$$E_{chem} = E_{rod+wat}^c - (E_{rod} + E_{wat}). \tag{2}$$

We show in Fig. 3 with circles the computed E_{chem} at different stresses. It is seen that E_{chem} will change from the positive values at low stresses to the negative ones at high stresses, indicating that chemisorption evolves from a thermodynamically unfavorable process to a favorable one with increasing stress. This trend is consistent with the concept of the stress-enhanced hydrolysis reaction from the thermodynamic perspective. Moreover, we fit the calculated chemisorption energy E_{chem} as a function of stress σ to quadratic order. The solid line in Fig. 3 is plotted according to the fitting formula given by

$$E_{chem} = 0.7004 - 0.0472\sigma - 0.0024\sigma^2, \tag{3}$$

where E_{chem} and σ are in unit of eV and GPa, respectively. Note that in Eq. (3), we use σ as the *labeling* variable, even though all our results are from *fixed-displacement* calculations. While the potential energy E is the appropriate thermodynamic potential for these calculations, and the nanorod strain ε should really be the independent variable, we think σ is more accessible and appealing to people since one sees the absolute magnitude of (nominal) stress to break bonds. The physical meaning of the coefficients in Eq. (3) as well as implications for understanding the effect of stress on the hydrolysis reaction will be discussed in Section 4.

3.3. Stress-dependent reaction pathways of hydrolysis

In transition from the initial to final state of chemical dissociation, three distinct reaction mechanisms are identified, each involving a different initiation process: (I) water dissociation, (II) water molecular chemisorption, and (III) direct siloxane bond breaking.

The first mechanism is characterized with the following sequence of reaction steps: (1) physisorption; (2) subsequent water dissociation including proton transfer and bond formation between Si–O_{wat}; and (3) final bond breaking between Si and bridging O_{br} of the siloxane bond. We show in Fig. 4 a series of snapshots along the reaction pathway at a stress of 16.7 GPa ($0.3\sigma_{cr}$). The corresponding location on the MEP for each frame is marked in Fig. 5. Atoms in Fig. 4 are color-coded according to the differences in atomic charge (Coulson charge calculated from MOPAC 2000) between the present value and the one at the initial state. Thus charge redistribution during the processes of bond breaking and formation can be revealed clearly. It is seen that as the water molecule approaches the nanorod, physisorption first occurs with the formation of two asymmetric hydrogen bonds as shown in Fig. 4(b). A small color variation indicates that there is only minuscule charge transfer associated with hydrogen bond formation. Then a concerted reaction occurs in which proton transfer to the bridging O_{br} is followed immediately with electron transfer from O_{wat} to Si atom. During this process, significant charge variation is observed as shown in the saddle-point configuration of Fig. 4(c). Specifically, as the bridging O_{br} forms a new bond with the incoming proton, it loses an electron and becomes positively charged. On the other hand, as Si atom forms a new bond with O_{wat}, it gains
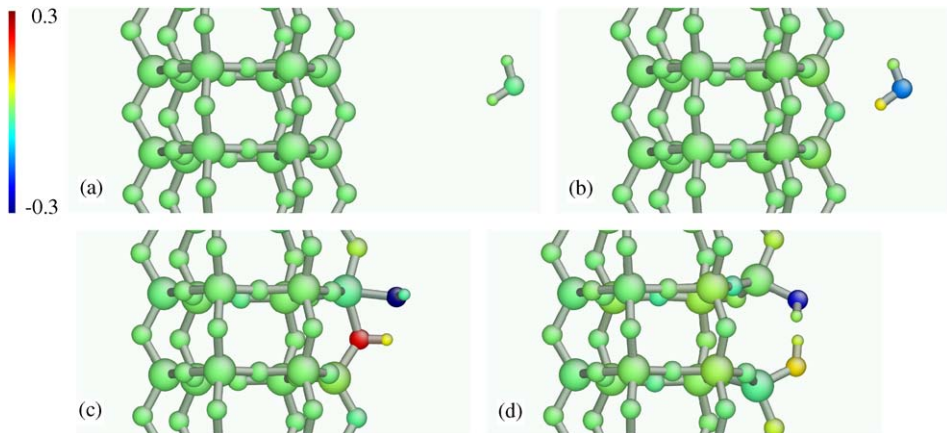

Fig. 4. Atomic configurations along the transition pathway of hydrolysis under a stress of $0.3\sigma_{cr}$. Mechanism I: (a) initial state, (b) physisorbed state, (c) saddle-point configuration, and (d) final chemisorbed state. Atoms are color-coded by charge variation relative to the initial configuration (a).
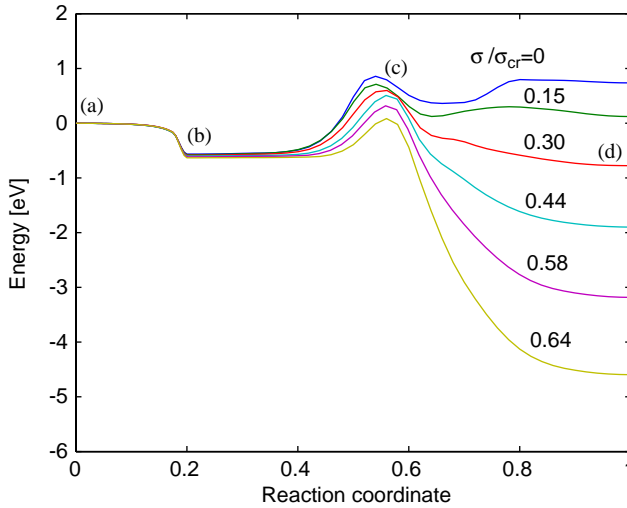
Fig. 5. Minimum energy paths of hydrolysis at different stresses: mechanism I.

electrons and thereby becomes negatively charged. The reaction is finally accomplished by forming two new silanol groups as shown in Fig. 4(d).

Fig. 5 shows the stress-dependent MEPs for the first reaction mechanism. While the nanorod is loaded with an incremental stretch of 0.5 Å, we parametrize MEPs according to the corresponding nominal stress, normalized by σ_{cr}. To facilitate comparison at different stress levels, we take the energy of the initial state as zero and plot the energy variation relative to the initial state as a function of the normalized reaction coordinate s. Here s is defined such that for any given extension of the nanorod, $s = 0$ represents the initial state at which the nanorod and water are non-interacting and $s = 1$ the final chemisorbed state. Within a $3N$ configurational space, where N is the total number of free atoms within the system, the hyperspace arc length along the MEP between the initial state $\mathbf{x}_i^{3N}$ and an intermediate state $\mathbf{x}^{3N}$ is given by

$$l \equiv \int_{\mathbf{x}_i^{3N}}^{\mathbf{x}^{3N}} \sqrt{d\mathbf{x}^{3N} \cdot d\mathbf{x}^{3N}}. \tag{4}$$

Then, the normalized reaction coordinate s is defined as

$$s \equiv \frac{l}{l_f}, \tag{5}$$

where l_f denotes the hyperspace arc length between the initial and final states. It is seen from Fig. 5 that in reference to the initial state, the energy at the saddle point as well as that at the final equilibrium state will decrease as the stress increases, indicating that the tensile stress assists the forward reaction both thermodynamically and kinetically. Then we extract the activation barrier from the saddle-point energy

on each MEP and plot it as a function of stress in Fig. 10 to compare with other mechanisms at the end of this subsection.

The second reaction mechanism is different from the first one in that a metastable, molecularly adsorbed state exists along the reaction pathway in going from the physisorbed to the final hydrolyzed state. We show in Fig. 6 snapshots along the reaction pathway at a stress of 16.7 GPa ($0.3\sigma_{cr}$) and plot in Fig. 7 MEPs at different stress levels. Similarly, the corresponding location on the MEP for each frame in Fig. 6 is also marked in Fig. 7. The atomic configuration of the molecularly adsorbed state which corresponds to a local minimum on the MEP is shown in Fig. 6(d). Note that this metastable state is absent on the MEP at zero stress and it starts to appear as the applied stress increases to about 5 GPa ($0.1\sigma_{cr}$). At this molecularly adsorbed state, Si atom adopts five-fold coordination and forms a new bond with O_{wat}. For example, the bond distance between Si and O_{wat} is 1.916 Å at a stress of 16.7 GPa ($0.3\sigma_{cr}$). This value falls into the range of an empirical chemical bond length. Due to the existence of such a metastable state on the MEP, there are two energy barriers that need to be overcome in going from the initial state to the final state of chemical dissociation. Two saddle-point configurations along the reaction pathway are shown in Fig. 6(c) and (e), respectively. The barrier height corresponding to each saddle
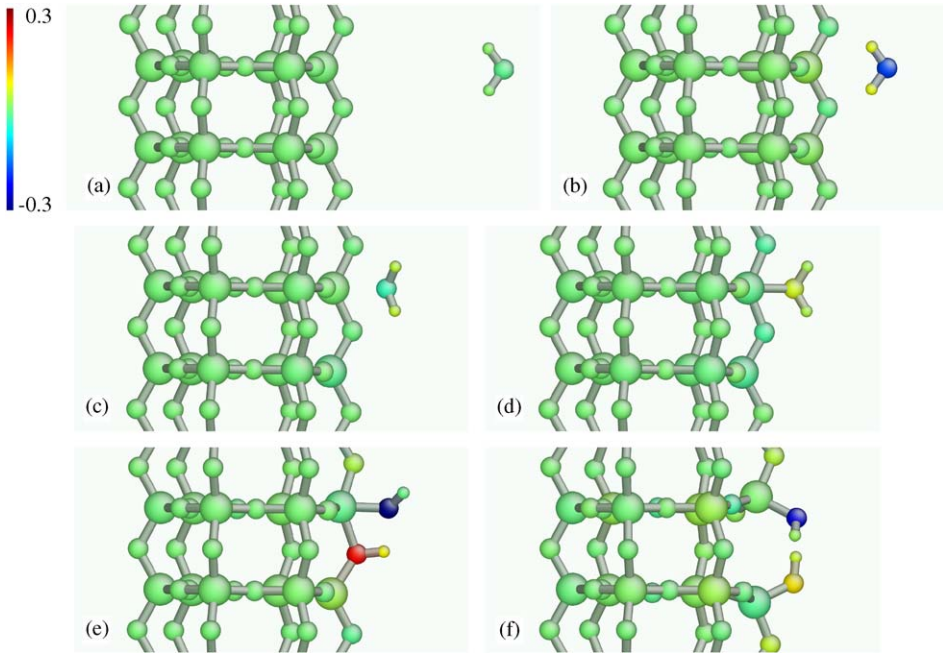

Fig. 6. Atomic configurations along the transition pathway of hydrolysis under a stress of $0.3\sigma_{cr}$. Mechanism II: (a) initial state, (b) physisorbed state, (c) the first saddle-point configuration, (d) metastable molecularly adsorbed state, (e) the second saddle-point configuration, and (f) final chemisorbed state. Atoms are color-coded by charge variation relative to the initial configuration (a).
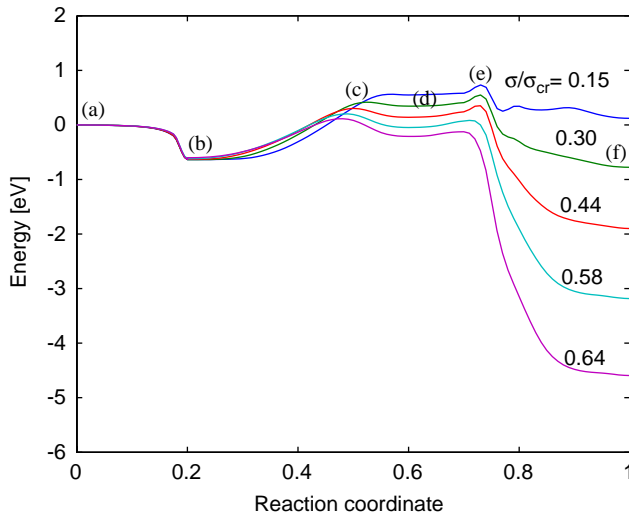
Fig. 7. Minimum energy paths of hydrolysis at different stresses: mechanism II.

point is also plotted in Fig. 10 as a function of stress. It is of interest to note that the two curves cross at a stress of about 27 GPa ($0.5\sigma_{cr}$). This crossing indicates that the rate-limiting step for the second reaction mechanism will switch from the process of water molecule dissociation followed by $Si–O_{wat}$ bond breaking at low stresses to the process of molecular binding of water with penta-coordinated Si at high stresses. We will compare the stress-dependent barrier heights with other mechanisms at the end of this subsection.

Lastly, the third reaction mechanism of hydrolyzing a strained nanorod is identified. This mechanism distinguishes itself from the other two in that the reaction first involves breaking the siloxane bond within the nanorod, and then terminating the dangling bond via the dissociated water molecule. Likewise, we show in Fig. 8 snapshots along the reaction pathway at a stress of 31.8 GPa ($0.58\sigma_{cr}$) and plot in Fig. 9 the calculated MEPs at different stress levels. The configuration close to the saddle point is shown in Fig. 8(c). It can be seen that the dangling O_{br} is being terminated by a proton transferring from a dissociated water molecule. For the third mechanism, the energy variation has a stronger dependence on the deformation state of the nanorod. Hence, we plot different MEPs in Fig. 9 at smaller stress intervals.

Fig. 10 compares the barrier height as a function of stress for the three different mechanisms of hydrolysis reaction. Evidently, the effect of tensile stress will reduce activation energy barrier for any specific reaction mechanism. More importantly, as the relative barrier height of different mechanisms changes with an increase in stress, the switching of rate-limiting steps will occur either within one type of reaction pathway, as discussed earlier for the second reaction mechanism, or among different reaction mechanisms. Thus, combining the results on the stress-mediated barrier height with those of the stress-dependent chemisorption energy, we obtain a
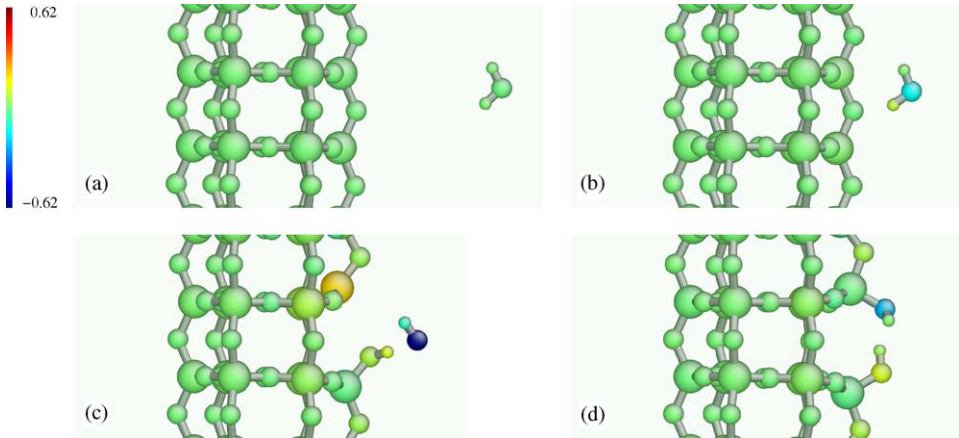
Fig. 8. Atomic configurations along the transition pathway of hydrolysis under a stress of $0.58\sigma_{cr}$. Mechanism III: (a) initial state, (b) physisorbed state, (c) saddle-point configuration, and (d) final chemisorbed state. Atoms are color-coded by charge variation relative to the initial configuration (a).
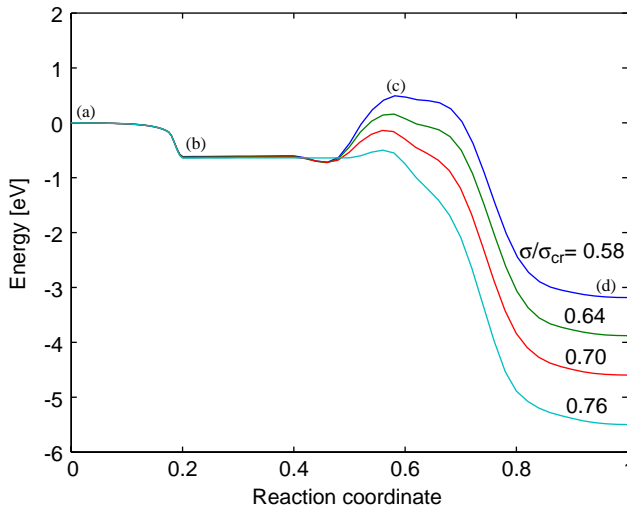

Fig. 9. Minimum energy paths of hydrolysis at different stresses: mechanism III.

complete picture of the stress-dependent hydrolysis reaction. Specifically, at the stress level below about 20% of the athermal strength σ_{cr}, the negative value of chemisorption energy indicates that the hydrolysis reaction is thermodynamically unfavorable. For the applied stress within 20–75% of σ_{cr}, the second reaction mechanism will be the rate-limiting process. Note that there will be a switching of the rate-limiting step within the pathway at about 50% of σ_{cr}. Finally, as the applied
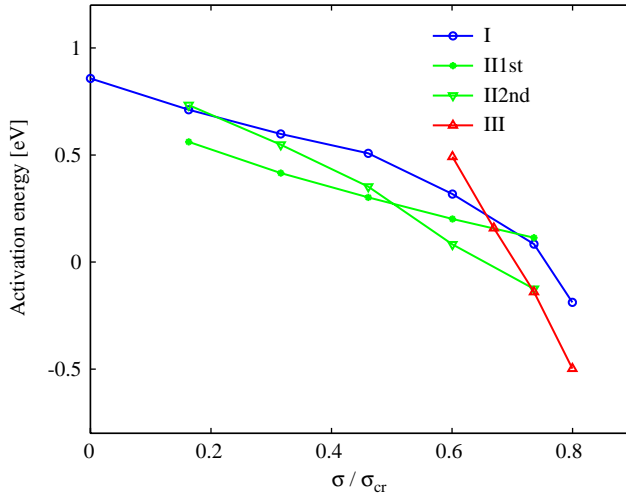
Fig. 10. Comparison of the stress-dependent activation barriers for the three molecular mechanisms of hydrolysis.

stress increases to above 75% of σ_{cr}, the third reaction mechanism will have the lowest activation energy barrier. However, the negative values of barrier height indicate that the reaction has become kinetically barrier-less.

3.4. Transition pathways of siloxane bond breaking in a dry nanorod

While the present study focuses on stress-dependent hydrolysis reaction, it is also of interest to compare the differences in breaking a siloxane bond with and without water. We show in Fig. 11 MEPs of breaking a siloxane bond in a dry nanorod at two representative stress levels, 31.8 GPa ($0.58\sigma_{cr}$) and 35.5 GPa ($0.64\sigma_{cr}$). It can be seen that when the stress is applied up to 31.8 GPa, the siloxane bond breaking without water is still thermodynamically unfavorable, while hydrolysis reactions under the same stress level are all thermodynamically favorable irrespective of the detailed transition mechanisms. Evidently, the presence of the water molecule facilitates the siloxane bond breaking. As the applied stress continues to increase, the MEP of breaking a siloxane bond without water evolves dramatically. When the stress is increased to 35.5 GPa, the corresponding MEP, as shown in Fig. 11, indicates that siloxane bond breaking becomes thermodynamically favorable with an activation energy barrier of about 0.6 eV. Fig. 12 shows the atomic configurations along the MEP at a stress of 31.8 GPa. It is seen that at the final state, there is a significant charge variation in association with the breaking of the siloxane bond. In contrast, the charge variation of the final hydrolyzed state shown in Figs. 4(d), 6(f) and 8(d) is relatively small because the dangling bonds are terminated by the dissociated water molecule.
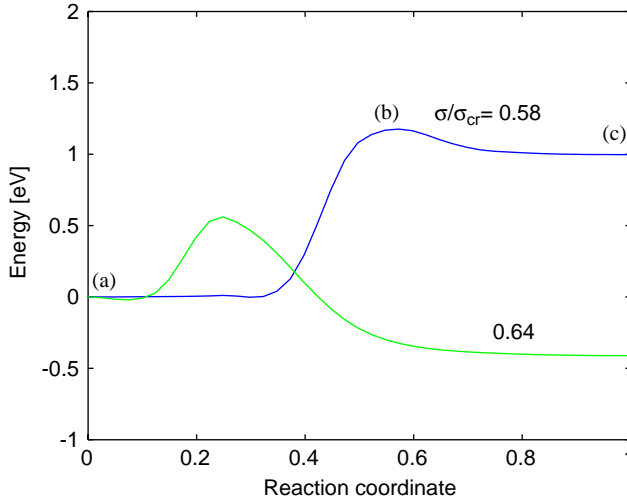
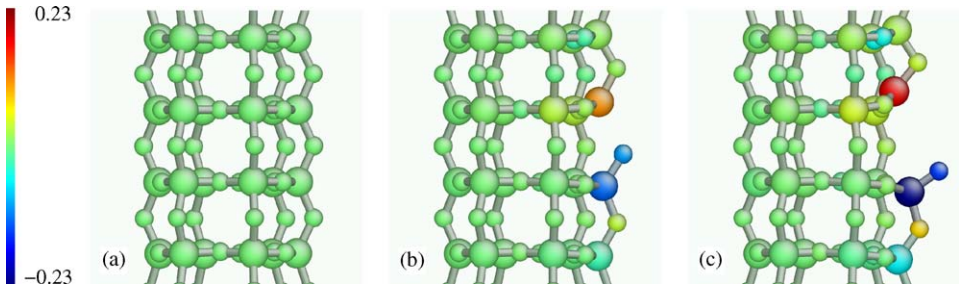Fig. 11. Minimum energy paths for breaking a siloxane bond in a dry nanorod.

Fig. 12. Snapshots along the transition pathway of siloxane bond breaking in a dry nanorod under the nominal stress of $35.5\,GPa$ ($0.64\sigma_{cr}$): (a) initial state, (b) saddle-point configuration, and (c) final chemisorbed state. Atoms are color-coded by charge variation relative to the initial configuration (a).

4. Analysis

In this section, we give an elementary analysis of the stress dependences of the thermodynamic driving force and kinetic barrier of chemical reactions, using the nanorod as a concrete test case. This is made possible by introducing a mechanically meaningful, continuous stress variable, which modulates chemical reactions near the nanorod surface. To our knowledge, it is the first time that such a quantitative analysis is carried out at the molecular level, although a similar approach has been taken to study the continuum inelastic deformation (see e.g. Rice, 1975; Argon, 1999). Our goals are to:

(1) Carefully analyze the crack extension driving force of brittle fracture when the effect of surface relaxation is significant, such as when foreign species are inserted

in the fracture process. Specifically, we find a term in the crack extension driving force that depends linearly on the external loading, which is absent in the conventional Griffith–Irwin analysis (Griffith, 1920; Irwin, 1957). Our numerical results indicate that this linear stress-dependent term in the crack extension driving force may play an important role in determining the Griffith condition of thermodynamic energy balance of brittle fracture for nano-sized systems.

(2) Provide a perturbation analysis of how the MEPs of chemical reactions are influenced by stress. Specifically, we will derive how the stationary points (initial, final and saddle-point states) of a MEP drift compared to $\sigma = 0$ counterparts. This would lead to perturbational expressions of how the thermodynamic driving force and kinetic barrier depend on stress, which in turn can be used to predict (a) at what stress level a certain reaction becomes favorable/unfavorable thermodynamically, (b) at what stress level there is a switch in the rate-controlling step (due to the competition between two saddles on the two distinct MEPs or between two saddles on the same MEP), (c) at what stress level the reaction can happen spontaneously without the aid of thermal fluctuations (see Li et al., 2002, for example).

We will first focus on the displacement-control loading condition. A brief discussion on the force-control condition will be given in Section 4.4 to contrast the differences.

4.1. Strain-dependent MEPs

Fig. 13 shows two schematic MEPs of hydrolysis for the nanorod at the extensions of zero and ΔL, respectively. When the nanorod is deformed, the energy of the system increases due to elastic energy injection. The local minima i on MEPs correspond to the initial states where the nanorod and single water molecule are non-interacting; the local minima f correspond to the final hydrolyzed states. Denote s as a reaction coordinate. Generally speaking, the locations of the initial/saddle-point/final states may all drift physically in the $\mathbf{x}^{3N}$ space at different load levels. But we choose our s-labeling scheme (like Eqs. (4) and (5)) such that $s = 0$ and 1 always
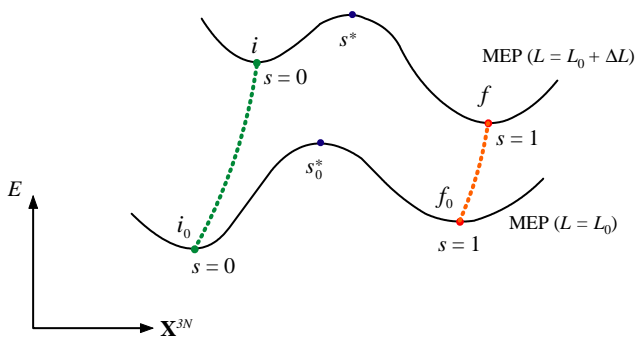

Fig. 13. Schematic of minimum energy paths at different load levels.

label the initial and final local equilibrium states. However, even then there is no guarantee that the saddle point in between would not drift in s. That is to say, in general $s^* \neq s_0^*$.

For any state s, the energy of the system at strain $\varepsilon = \Delta L / L_0$ can be related to that at $\varepsilon = 0$ by

$$E(\varepsilon, s) \equiv E(0, s) + \sigma_0(s)\varepsilon V_0 + \tfrac{1}{2}k_0(s)\varepsilon^2 V_0 + \mathcal{O}(\varepsilon^3), \tag{6}$$

where $V_0 = A_0 L_0$ is the nominal volume of the nanorod at $(\varepsilon = 0, s = 0)$, $\sigma_0(s)$ is the residual stress within the nanorod at $(\varepsilon = 0, s)$, and $k_0(s)$ is the nanorod stiffness at $(\varepsilon = 0, s)$. Eq. (6) can be considered as the definition of $\sigma_0(s)$ and $k_0(s)$. Since we have chosen the initial state at $\varepsilon = 0$ to be stress free, $\sigma_0(0) = 0$ holds.

The values of $k_0(0)$, $\sigma_0(1)$ and $k_0(1)$ can be directly read off from Fig. 2. For $s = 0$ and 1, $k_0(s)$ can be understood operationally as the stiffness of pulling the two end grips of the nanorod, but allowing everything inside (with water fragments at $s = 1$, without at $s = 0$) to relax locally. When $0 < s < 1$, the physical interpretation of $k_0(s)$ is not so straightforward and depends numerically on the definition of s.

Denote $\Delta E(\varepsilon, s)$ as the change of the energy in going from the initial state i to an intermediate state s when holding the nanorod extension fixed. From Eq. (6), one obtains

$$\begin{aligned}
\Delta E(\varepsilon, s) &\equiv E(\varepsilon, s) - E(\varepsilon, 0) \\
&= \Delta E(0, s) + \sigma_0(s)\varepsilon V_0 + \tfrac{1}{2}\Delta k_0(s)\varepsilon^2 V_0 + \mathcal{O}(\varepsilon^3),
\end{aligned} \tag{7}$$

where $\Delta k_0(s)$ denotes the stiffness change from state i to s, i.e., $\Delta k_0(s) \equiv k_0(s) - k_0(0)$. It is seen from Eq. (7) that the energy variation in going from state i to s at a fixed ε can be partitioned into strain-independent and strain-dependent contributions. The former represented by the term $\Delta E(0, s)$ is the energy difference between state s and i at zero strain. For the strain-dependent part, the linear term in ε arises from the residual stress $\sigma_0(s)$ in association with a partially hydrolyzed nanorod at zero strain, while the term quadratic in ε results from the change of the nanorod stiffness when a siloxane bond is partially broken.

4.2. Thermodynamic driving force for hydrolysis reaction

With the general expression Eq. (7), we first consider the energy difference between two local equilibrium states i and f. As $\Delta E(\varepsilon, 1)$ represents the energy increase in going from the initial to final state, its negative value can be interpreted as the thermodynamic driving force $D(\varepsilon)$ for a forward transition. That is,

$$\begin{aligned}
D(\varepsilon) &\equiv -\Delta E(\varepsilon, 1) \\
&= -\Delta E(0, 1) - \sigma_0(1)\varepsilon V_0 - \tfrac{1}{2}\Delta k_0(1)\varepsilon^2 V_0 + \mathcal{O}(\varepsilon^3).
\end{aligned} \tag{8}$$

The physical meaning of each term in the second step of Eq. (8) can be understood as follows: $\Delta E(0, 1)$ is the energy change associated with reaction at zero strain. Our calculation indicates that this strain-independent energy term is greater than zero for the hydrolysis reaction. Hence it can be regarded as the internal resistance to the

reaction. As the two newly formed silanol surface groups repel each other, the residual stress $\sigma_0(1)$ is compressive when we hold fixed the two ends of the nanorod, i.e., $\sigma_0(1) < 0$. In addition, the nanorod stiffness will decrease when a strong siloxane bond is replaced by a pair of weakly interacting silanol groups, i.e., $\Delta k_0(1) < 0$. Hence in Eq. (8), both the linear and the quadratic terms in ε will contribute to an increase in the driving force $D(\varepsilon)$.

To write the driving force D in terms of the nominal stress, we note that

$$\varepsilon = \frac{\sigma}{k_0(0)} + \frac{\sigma^2}{2S(0)} + \mathcal{O}(\sigma^3), \tag{9}$$

where $S(0)$ is the softening coefficient when we stretch the $s = 0$ nanorod. Plugging Eq. (9) into Eq. (8), we have

$$D(\sigma) = -\Delta E(0,1) - \frac{\sigma_0(1)}{k_0(0)}\sigma V_0 - \frac{1}{2}\left[\frac{\Delta k_0(1)}{[k_0(0)]^2} + \frac{\sigma_0(1)}{S(0)}\right]\sigma^2 V_0 + \mathcal{O}(\sigma^3). \tag{10}$$

Comparing with Eq. (3), we can estimate the values of both the residual stress $\sigma_0(1)$ and the change in the nanorod stiffness $\Delta k_0(1)$ once the initial stiffness $k_0(0)$ and softening coefficient $S(0)$ are known. For the present nanorod system, the values of $k_0(0) = 189\,\text{GPa}$ and $S_0(0) = 8.9 \times 10^4\,\text{GPa}^2$ lead to the estimated $\sigma_0(1) = -1.51\,\text{GPa}$ and $\Delta k_0(1) = -28\,\text{GPa}$, close to the result from a direct calculation, $\sigma_0(1) = -1.5\,\text{GPa}$ and $\Delta k_0(1) = -35\,\text{GPa}$.

To prepare for the discussion on the stress-dependence of crack extension driving force in the next subsection, we also calculate the critical condition when the thermodynamic driving force of hydrolysis reaction vanishes. In other words, we want to determine the critical load above which the forward transition of bond breaking becomes thermodynamically favorable. From Eq. (3), the critical load σ is determined to be 9.88 GPa. To demonstrate the importance of the linear stress-dependence, we intentionally drop the linear term in Eq. (3) and then recalculate the critical load. This corresponds to a situation where the effect of the linear stress-dependent term is not taken into account. The critical value of σ then becomes 17.1 GPa. Evidently, there is a significant difference in the estimated critical load (about 73%) if the linear stress-dependent term is ignored.

4.3. Implications for brittle fracture analysis

The analysis of energy change associated with nanorod bond breaking can help elucidate the thermodynamic driving force of brittle fracture. The existing understanding of brittle fracture at the atomic scale was obtained by introducing the concept of "lattice trapping" (the fracture analogue of the Peierls resistance to dislocation motion) (see Thomson et al., 1971). Here, we briefly review this concept and more detailed discussions on this topic can be found in, e.g., Lawn (1993), Marder (1996) and Zhu et al. (2004). Consider a simplified model system with an atomically sharp crack embedded in an otherwise perfect 2D lattice. The quasi-static crack growth corresponds to a sequence of localized bond-breaking processes at the instantaneous crack tip. Under a given external load, the total energy of the system

can be written as a function of crack length. Because of lattice discreteness, the energy landscape corrugates at the atomic scale along the crack extension direction. As a result, crack extension may cease temporarily when the system is trapped in a well of the energy surface; an activation energy is required to overcome the local energy barrier (Zhu et al., 2004). Each time the crack extends by one lattice spacing, the system will move from one state of local energy minimum to an adjacent one. The energy difference between the two local energy-minimum states determines the instantaneous thermodynamic driving force of crack extension by one lattice spacing, and the local maximum in between gives the activation energy barrier which determines the instantaneous kinetic rate of crack growth.

A connection between lattice trapping at a crack tip and bond breaking in a nanorod can be established if we regard the breaking of a siloxane bond in a perfect nanorod as effectively creating a small notch crack. The targeted siloxane bond can also be thought as being lattice-trapped. Although the detailed atomic structure and stress state are different for the two situations, we believe that the general trend revealed by the study of the nanorod bond breaking will be instructive for understanding the hydrolysis reaction at the crack tip.

Now suppose a single siloxane bond occupies an effective area ΔA; we may write the crack extension driving force as

$$D(\varepsilon) = [\mathscr{G}(\varepsilon) - 2\gamma_s^u]\Delta A, \tag{11}$$

where the strain-dependent terms in Eq. (8) are lumped together to give the energy release rate

$$\mathscr{G}(\varepsilon) = -\frac{\sigma_0(1)\varepsilon V_0 + \frac{1}{2}\Delta k_0(1)\varepsilon^2 V_0}{\Delta A} \tag{12}$$

and the strain-independent term, corresponding to the energy variation in association with fracture at zero strain, is the unrelaxed surface energy γ_s^u. That is,

$$\gamma_s^u = \frac{\Delta E(0,1)}{2\Delta A}. \tag{13}$$

It is commonly held that for a brittle crack in a linear elastic continuum, the energy release rate $\mathscr{G}(\varepsilon)$ is only a function of ε^2 (see Lawn, 1993, for example). But the energy release rate $\mathscr{G}(\varepsilon)$ given in Eq. (12) contains a linear term in ε, related to the residual stress after fracture due to surface creation and insertion of foreign species. We have numerically demonstrated, in Section 4.2, this linear term is important in determining the Griffith condition of energy balance before and after bond breaking in the case of the nanorod fracture. Then a question arises: under what conditions should the linear driving force term be taken into account in studying brittle crack propagation?

To address the above question, we perform a thought experiment by considering an infinitely long strip with clamped boundaries having fixed vertical displacement δ_{ext} (see Fig. 14). Suppose the slab is under a plane-stress condition, and a crack exists along the x_1 direction. Since the crack propagation is translationally invariant along x_1, the driving force for creating a new surface area ΔA at the crack tip can be
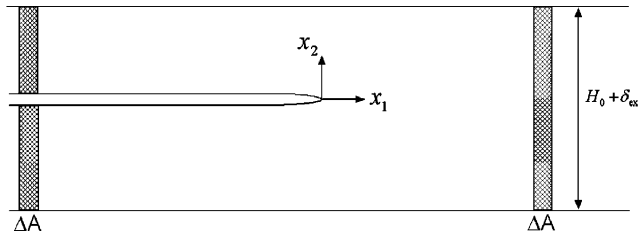
Fig. 14. Schematic of an infinitely long cracked strip with a height of H_0; a displacement δ_{ext} is imposed on the boundary.

simply calculated by the energy difference between slabs of cross-sectional area ΔA upstream and downstream; the two slabs are schematically represented by shaded blocks in Fig. 14. We write the driving force D as

$$D(\varepsilon) \equiv \Delta E_{+\infty} - \Delta E_{-\infty}. \tag{14}$$

In Eq. (14), strain $\varepsilon = \delta_{\text{ext}}/H_0$, where H_0 denotes the length of the relaxed slab; $\Delta E_{+\infty}$ is the elastic energy stored in the slab upstream,

$$\Delta E_{+\infty} = \tfrac{1}{2}K\delta_{\text{ext}}^2, \tag{15}$$

where the stiffness of the slab K is related to Young's modulus Y by

$$K = \frac{Y\Delta A}{H_0}, \tag{16}$$

$\Delta E_{-\infty}$ is the energy stored in the slab downstream. This slab has fractured into two pieces with a newly created cross-sectional area ΔA. Suppose there is a surface displacement (expansion), denoted by δ_{s}, in association with fracture, which arises either due to surface reconstruction or surface reaction with foreign molecules.

When $\delta_{\text{ext}} = \delta_{\text{s}}$, the interaction between the two fractured surfaces vanishes. The excess energy of the fractured slab is twice the relaxed surface energy $\gamma_{\text{s}}^{\text{r}}\Delta A$. Here, we have taken the energy of the relaxed slab (no fracture) as a reference. The value of $\gamma_{\text{s}}^{\text{r}}$ approaches the macroscopic relaxed surface energy when H_0 is sufficiently large.

When $\delta_{\text{ext}} < \delta_{\text{s}}$, a compressive force of $F_{\text{s}} = \tilde{K}(\delta_{\text{s}} - \delta_{\text{ext}})$ exists in the slab, where $\tilde{K}$ denotes the effective stiffness of the fractured slab. Since the two newly created surfaces still interact with each other through the terminated silanol groups, $\tilde{K}$ differs from K. This difference becomes negligible when H_0 is sufficiently large. The energy in the fractured slab $\Delta E_{-\infty}$ can be written as

$$\Delta E_{-\infty} = \tfrac{1}{2}\tilde{K}(\delta_{\text{ext}} - \delta_{\text{s}})^2 + 2\gamma_{\text{s}}^{\text{r}}\Delta A. \tag{17}$$

In the limit of $\delta_{\text{ext}} = 0$, $\Delta E_{-\infty}$ is twice the unrelaxed surface energy according to the definition of Eq. (13). Then, we have

$$\gamma_{\text{s}}^{\text{u}} = \frac{1}{4\Delta A}\tilde{K}\delta_{\text{s}}^2 + \gamma_{\text{s}}^{\text{r}}. \tag{18}$$

Substitution of Eqs. (15), (17) and (18) into Eq. (14), one obtains

$$D(\delta_{\text{ext}}) = \tilde{K}\delta_s\delta_{\text{ext}} + \tfrac{1}{2}(K - \tilde{K})\delta_{\text{ext}}^2 - 2\gamma_s^{\text{u}}\Delta A. \tag{19}$$

In Eq. (19), the crack extension driving force consists of both the linear and quadratic terms in the applied load, given in terms of the boundary displacement δ_{ext}. It is readily to identify the corresponding terms between Eq. (19) and Eqs. (11)–(13). Note that Eq. (19) is only valid when the condition of $\delta_{\text{ext}} \leqslant \delta_s$ is satisfied, where the surface displacement δ_s is normally of the order of lattice constant a_0.

When $\delta_{\text{ext}} > \delta_s$, the two fractured surfaces cease to interact with each other. That is, δ_s represents a cut-off distance beyond which the interaction is considered negligible. Then, the excess energy in the fractured slab is a constant corresponding to twice the relaxed surface energy $\gamma_s^{\text{r}}\Delta A$, Thus, the driving force only contains the term quadratic in δ_{ext}. That is,

$$D(\delta_{\text{ext}}) = \tfrac{1}{2}K\delta_{\text{ext}}^2 - 2\gamma_s^{\text{r}}\Delta A. \tag{20}$$

In addition, within the regime of $\delta_{\text{ext}} < \delta_s$, a further requirement on the system size can be derived from the Griffith condition of fracture propagation. That is, the system under a displacement load of δ_{ext} should provide a sufficient driving force to overcome the fracture resistance. Consider the following scaling relation: the driving force term $\tilde{K}\delta_s\delta_{\text{ext}} \sim Ya_0^2\Delta A/H_0$, where $\sim$ means "of the order of". Here, we have taken the limit of $\delta_{\text{ext}} \sim \delta_s \sim a_0$. The surface creation resistance $\gamma_s^{\text{r}}\Delta A \sim Ya_0/10\Delta A$. To balance the above two terms of $\tilde{K}\delta_s\delta_{\text{ext}}$ and $\gamma_s^{\text{r}}\Delta A$, we obtain $H_0 \sim 10a_0$. Since a_0 is of the order of angstrom, this condition essentially requires that the system size needs to be on the nanoscale in order to fracture the system under a displacement load of the order of a_0. Considering the two constraints derived above, i.e., $\delta_{\text{ext}} < \delta_s$ and $H_0 \sim 10a_0$, we conclude that this linear driving force term is only important in determining the critical condition of brittle fracture initiation for nanosized systems.

4.4. Stationary-point drift

In this subsection, we first provide a perturbation analysis of the stationary-point drift on the MEP for a generically defined reaction coordinate s. Then we apply this general result to analyze the external-load dependence of the activation barrier for the specific scheme of defining the reaction coordinate employed in this work, i.e., both the reaction coordinates of the initial and final states are fixed by definition.

Denote s_0^* as the reaction coordinate of one stationary point (local minimum or saddle point) on the MEP at zero strain. For a point s near s_0^* on the same MEP, the energy at zero strain is given by

$$E(0, s) = E(0, s_0^*) + \tfrac{1}{2}\kappa_0(s_0^*)(s - s_0^*)^2 V_0 + \mathcal{O}((s - s_0^*)^3), \tag{21}$$

where $\kappa_0(s)$ denotes the local curvature at s and it is given by

$$\kappa_0(s) \equiv \frac{\partial^2 E(0, s)}{\partial s^2}. \tag{22}$$

Consider state s on the MEP at strain ε. Substitution of Eq. (21) into Eq. (6) gives a relation between the energy at the point (ε, s) to that at $(0, s_0^*)$,

$$E(\varepsilon, s) = E(0, s_0^*) + \tfrac{1}{2}\kappa_0(s_0^*)(s - s_0^*)^2 V_0 + \sigma_0(s)\varepsilon V_0 + \tfrac{1}{2}k_0(s)\varepsilon^2 V_0$$
$$+ \mathcal{O}((s - s_0^*)^3) + \mathcal{O}(\varepsilon^3). \tag{23}$$

Denote s^* as the saddle point on the MEP at strain ε,

$$\left.\frac{\partial E(\varepsilon, s)}{\partial s}\right|_{s=s^*} = 0. \tag{24}$$

Substituting Eq. (23) into Eq. (24), one obtains

$$\kappa_0(s_0^*)(s^* - s_0^*) + \sigma_0'(s^*)\varepsilon + \tfrac{1}{2}k_0'(s^*)\varepsilon^2 = \mathcal{O}((s - s_0^*)^2) + \mathcal{O}(\varepsilon^3), \tag{25}$$

where the prime denotes derivative with respect to s. Solving Eq. (25) to the leading order in ε and $s^* - s_0^*$, s^* deviates from s_0^* by

$$s^* = s_0^* - \frac{\sigma_0'(s_0^*)}{\kappa_0(s_0^*)}\,\varepsilon + \mathcal{O}(\varepsilon^2). \tag{26}$$

Eq. (26) gives the leading-order estimate about stationary-point drift based on the information at s_0^* on the MEP of zero strain.

For a particular scheme of defining the reaction coordinate s that consistently labels the initial equilibrium state as $s = 0$ and the final equilibrium state as $s = 1$ (such as the Eqs. (4) and (5) scheme), there are by definition zero stationary-point drifts for these two special points. Thus, one must have

$$\sigma_0'(s_0^* = 0) = 0, \quad \sigma_0'(s_0^* = 1) = 0, \tag{27}$$

as constraints on the labeling scheme.

Substitution of Eq. (26) into Eq. (23) gives the connection between stationary-point energies at strain ε and strain zero. That is,

$$E(\varepsilon, s^*) = E(0, s_0^*) + \sigma_0(s_0^*)\varepsilon V_0 + \frac{1}{2}\left[k_0(s_0^*) - \frac{\sigma_0'^2(s_0^*)}{\kappa_0(s_0^*)}\right]\varepsilon^2 V_0 + \mathcal{O}(\varepsilon^3). \tag{28}$$

Denote s_0^{sad} as the reaction coordinate of a saddle-point state on the MEP of zero strain. From Eq. (28), the activation energy $\Delta E(\varepsilon)$ at strain ε is related to the activation energy ΔE_0 at zero strain by

$$\Delta E(\varepsilon) = \Delta E_0 + \Delta\sigma_0(s_0^{\mathrm{sad}})\varepsilon V_0 + \frac{1}{2}\left[k_0(s_0^{\mathrm{sad}}) - k_0(0) - \frac{\sigma_0'^2(s_0^{\mathrm{sad}})}{\kappa_0(s_0^{\mathrm{sad}})}\right]\varepsilon^2 V_0 + \mathcal{O}(\varepsilon^3). \tag{29}$$

Note that by definition we have chosen the initial state at $\varepsilon = 0$ to be stress free, i.e., $\sigma_0(0) = 0$. We have also made use of Eq. (27). From Eq. (29), the activation energy $\Delta E(\varepsilon)$ at strain ε can be estimated using the information obtained from the MEP of zero strain. In practice, we have to make a few more calculations beyond the MEP of

zero strain in order to estimate the higher order quantities such as the stiffness of the system. Nevertheless, this perturbation analysis reveals the physical origin of the external-load dependence in modulating the kinetic barriers of reaction. By evaluating Eq. (29) for two distinct saddles with the same initial state (the two saddles may or may not be on the same MEP), we can predict at what stress a cross-over in $\Delta E(\varepsilon)$ will occur like those shown in Fig. 10, at which point the rate-controlling microscopic reaction step or mechanism switches.

4.5. Stress-dependent MEP

While the above analysis is given using the tensile strain of the nanorod as a control variable, the derivation procedure and results on the strain-dependent thermodynamic driving force and activation energy barriers can be easily adapted to the stress-controlled situation. When the nanorod is stretched under stress control, the total energy of the system $G(\sigma, s)$ includes contributions from both the atomic configuration energy and the potential energy of the load, i.e., $G = E - \sigma \varepsilon V_0$. Following the same scheme of labeling various states on the MEPs as that discussed in Section 4.1, in parallel to Eq. (7), the energy at stress σ is related to that at zero stress by

$$\Delta G(\sigma, s) = \Delta G(0, s) + \varepsilon_0(s)\sigma V_0 - \tfrac{1}{2}\Delta c_0(s)\sigma^2 V_0, \qquad (30)$$

where $\varepsilon_0(s)$ is the strain in the nanorod due to the hydrolysis reaction at zero stress, $\Delta c_0(s)$ is the compliance change from state i to s. That is, $\Delta c_0(s) \equiv c_0(s) - c_0(0)$, where $c_0(s)$ is the compliance of nanorod at an intermediate state s, and it is the inverse of the stiffness $k_0(s)$.

The connection between the two loading conditions on energy change can be seen when Eq. (7) is rewritten in terms of the nominal stress σ, where σ is related to the nominal strain by $\sigma = k_0(0)\varepsilon$. That is,

$$\Delta E(\varepsilon, s) = \Delta E(0, s) + \frac{\sigma_0(s)}{k_0(s)}\frac{k_0(s)}{k_0(0)}\,\sigma V_0 - \frac{1}{2}\frac{k_0(s)}{k_0(0)}\,\Delta c_0(s)\sigma^2 V_0. \qquad (31)$$

Comparing Eq. (31) with Eq. (30), it is seen that if the stiffness change at state s is small relative to the initial stiffness $k_0(0)$, i.e., $k_0(s)/k_0(0)\sim 1$, Eqs. (31) and (30) will be equivalent because the relations $\varepsilon_0(s) = \sigma_0(s)/k_0(s)$ and $\Delta E(0, s) = \Delta G(0, s)$ always hold. Therefore, as a first approximation, the energy variation associated with bonding breaking is independent of the type of boundary conditions imposed. This is reminiscent of a well-known result in fracture mechanics. That is, the energy release rate for crack extension is independent of loading methods. However, for a finite size system such as a nanorod, there are only six siloxane bonds intersecting each cross-sectional plane of the nanorod. Breaking a single bond will approximately reduce the effective tension stiffness of the nanorod by one sixth. Because of this significant stiffness change, the effect of different loading methods is expected to be appreciable. In the future, it would be of interest to quantitatively evaluate the size effect on the present molecular study regarding the stress dependence of thermodynamics and kinetics of chemical reaction.

5. Summary

In this paper, the stress dependence of a water–silica reaction is calculated for a model system. Both the thermodynamic driving force and activation barrier reveal interesting features. For the former, we found a linear stress-dependent contribution that is absent in the classic analysis of energy release rate, which was decomposed into surface creation (zeroth order in stress) and change in effective compliance (second-order in stress) contributions, as the crack advances by a unit spacing. This linear driving force term is formalistically and numerically shown to be related to the relaxation displacement associated with surface creation, which is especially significant for nano-sized systems when foreign species are inserted in the fracture process. For the activation barrier of reaction, we applied the nudged elastic band method to map out the MEPs, and found stress-dependent saddle-point energies. We then developed perturbation theories to describe how the saddle points drift in both reaction coordinate and energy as stress is varied. This formulation reveals the physical origin of the stress dependence of kinetic barrier; and it allows one to extrapolate, from near zero stress calculations, how different saddle points compete (at what stress level a crossing in saddle energy will likely occur), when a saddle will vanish, etc. Even though with a special labeling scheme, the initial and final states do not drift in reaction coordinate, they do drift in energies. Our perturbation theory on stationary-point drifts also predicts at what stress the reaction becomes favorable thermodynamically, and at what stress the reaction can proceed without requiring thermal activation to overcome a barrier.

Acknowledgements

References

Argon, A.S., 1999. Rate processes in plastic deformation of crystalline and noncrystalline solids. In: Meyers, M.A., Armstrong, R.W., Kirchner, H. (Eds.), Mechanics and Materials: Fundmentals and Linkages. Wiley, New York, pp. 175–230.

Chuang, T.J., Fuller, E.R., 1992. Extended Charles–Hillig theory for stress corrosion cracking of glass. J. Am. Ceram. Soc. 75, 540–545.

de Leeuw, N.H., Du, Z., Li, J., Yip, S., Zhu, T., 2003. Computer modeling study of the effect of hydration on the stability of a silica nanotube. Nano Lett. 3, 1347–1352.

Du, M.H., Kolchin, A., Cheng, H.P., 2003. Water–silica surface interactions: A combined quantum-classical molecular dynamic study of energetics and reaction pathways. J. Chem. Phys. 119, 6418–6422.

Gilman, J.J., 2003. Electronic Basis of the Strength of Materials. Cambridge University Press, Cambridge.

Griffith, A.A., 1920. The phenomena of rupture and flow in solids. Philos. Trans. R. Soc. London A 221, 163–198.

Henkelman, G., Jónsson, H., 2000. Improved tangent estimate in the nudged elastic band method for finding minimum energy paths and saddle points. J. Chem. Phys. 113, 9978–9985.

Hillig, W.B., Charles, R.J., 1964. Surfaces, stress-dependent surface reactions, and strength. In: Zackay, V.F. (Ed.), High-Strength Materials. Wiley, New York, pp. 682–705.

Irwin, G.R., 1957. Analysis of stresses and strains near the end of a crack traversing a plate. J. Appl. Mech. 24, 361–364.

Jónsson, H., Mills, G., Jacobsen, K.W., 1998. Nudged elastic band method for finding minimum energy paths of transitions. In: Berne, B.J., Ciccotti, G., Coker, D.F. (Eds.), Classical and Quantum Dynamics in Condensed Phase Simulations. World Scientific, Singapore, pp. 385–404.

Kim, C.C., Bell, M.I., McKeown, D.A., 1995. Virbrational analysis of beryl ($Be_3Al_2Si_6O_{18}$) and its constituent ring (Si_6O_{18}). Physica B 205, 193–208.

Kurkjian, C.R., Gupta, P.K., Brow, R.K., Lower, N., 2003. The intrinsic strength and fatigue of oxide glasses. J. Non-Cryst. Solids 316, 114–124.

Laurence, P.R., Hillier, I.H., 2003. Towards modeling bioactive glasses: Quantum chemistry studies of the hydrolysis of some silicate structures. Comput. Mater. Sci. 28, 63–75.

Lawn, B.R., 1993. Fracture of Brittle Solids, second ed. Cambridge University Press, Cambridge.

Li, J., Van Vliet, K.J., Zhu, T., Yip, S., Suresh, S., 2002. Atomistic mechanisms governing elastic limit and incipient plasticity in crystals. Nature 418, 307–310.

Liao, D.Y., 2001. Atomistic simulation of strength and deformation of ceramic materials. MIT Thesis, p. 98.

Lindsay, C.G., White, G.S., Freiman, S.W., Wong-Ng, W., 1994. Molecular orbital study of an environmentally enhanced crack growth process in silica. J. Am. Ceram. Soc. 77, 2179–2187.

Marder, M., 1996. Statistical mechanics of cracks. Phys. Rev. E 54, 3442–3454.

Michalske, T.A., Bunker, B.C., 1984. Slow fracture model based on strained silicate structures. J. Appl. Phys. 56, 2686–2693.

Michalske, T.A., Freiman, S.W., 1982. A molecular interpretation of stress corrosion in silica. Nature 295, 511.

Michalske, T.A., Freiman, S.W., 1983. A molecular mechanism for stress corrosion in vitreous silica. J. Am. Ceram. Soc. 66, 284–288.

Orowan, E., 1944. The fatigue of glass under stress. Nature 154, 341–343.

Proctor, B.A., Whitney, I., Johnson, J.W., 1967. The strength of fused silica. Proc. R. Soc. A 297, 534–557.

Rice, J.R., 1975. Continuum mechanics and thermodynamics of plasticity in relation to microscale deformation mechanisms. In: Argon, A.S. (Ed.), Constitutive Equations in Plasticity. MIT Press, Cambridge, MA, pp. 23–79.

Rice, J.R., 1978. Thermodynamics of the quasi-static growth of Griffith cracks. J. Mech. Phys. Solids 26, 61–78.

Sorensen, M.R., Mishin, Y., Voter, A.F., 2000. Diffusion mechanisms in Cu grain boundaries. Phys. Rev. B 62, 3658–3673.

Stewart, J.J.P., 1989. Optimization of parameters for semi-empirical methods I-Method. J. Comput. Chem. 10, 209–220.

Stewart, J.J.P., 2002. MOPAC 2002 User's Manual. Fujitsu Limited, Tokyo, Japan.

Thomson, R., Hsieh, C., Rana, V., 1971. Lattice trapping of fracture cracks. J. Appl. Phys. 42, 3145–3160.

Vineyard, G.H., 1957. Frequency factors and isotope effects in solid state rate processes. J. Phys. Chem. Solids 3, 121–127.

Walsh, T.R., Wilson, M., Sutton, A.P., 2000. Hydrolysis of the amorphous silica surface. II. Calculation of activation barriers and mechanisms. J. Chem. Phys. 113, 9191–9201.

West, J.K., Hench, L.L., 1994. Silica fracture, part II. A ring-opening model via hydrolysis. J. Mater. Sci. 29, 5808–5816.

Wiederhorn, S.M., 1967. Influence of water vapor on crack propagation in soda-lime glass. J. Am. Ceram. Soc. 50, 407–414.

Zhu, T., Li, J., Yip, S., Bartlett, R.J., Trickey, S.B., deLeeuw, N.H., 2003. Deformation and fracture of a SiO_2 nanorod. Mol. Simulat. 29, 671–676.

Zhu, T., Li, J., Yip, S., 2004. Atomistic configurations and energetics of crack extension in silicon. Phys. Rev. Lett. 93, 205504.

Zhu, W.M., Taylor, C., Al-Derzi, A.R., Runge, K., Trickey, S.B., Zhu, T., Li, J., Yip, S., 2005. Molecular dynamics tests of electronic structure encoding in pair potentials for SiO_2, submitted for publication.